

Magnonic interferometric switch for multi-valued logic circuits

Michael Balynsky,¹ Alexander Kozhevnikov,² Yuri Khivintsev,^{2,3} Tonmoy Bhowmick,¹ David Gutierrez,¹ Howard Chiang,¹ Galina Dudko,² Yuri Filimonov,^{2,3} Guanxiong Liu,¹ Chenglong Jiang,¹ Alexander A. Balandin,¹ Roger Lake,¹ and Alexander Khitun¹

¹Department of Electrical and Computer Engineering, University of California-Riverside, Riverside, California 92521, USA

²Kotelnikov Institute of Radioengineering and Electronics of the Russian Academy of Sciences, Saratov 410019, Russia

³Saratov State University, Saratov 410012, Russia

(Received 27 September 2016; accepted 1 December 2016; published online 13 January 2017)

We investigated a possible use of the magnonic interferometric switches in multi-valued logic circuits. The switch is a three-terminal device consisting of two spin channels where input, control, and output signals are spin waves. Signal modulation is achieved via the interference between the source and gate spin waves. We report experimental data on a micrometer scale prototype based on the $Y_3Fe_2(FeO_4)_3$ structure. The output characteristics are measured at different angles of the bias magnetic field. The On/Off ratio of the prototype exceeds 13 dB at room temperature. Experimental data are complemented by the theoretical analysis and the results of micro magnetic simulations showing spin wave propagation in a micrometer size magnetic junction. We also present the results of numerical modeling illustrating the operation of a nanometer-size switch consisting of just 20 spins in the source-drain channel. The utilization of spin wave interference as a switching mechanism makes it possible to build nanometer-scale logic gates, and minimize energy per operation, which is limited only by the noise margin. The utilization of phase in addition to amplitude for information encoding offers an innovative route towards multi-state logic circuits. We describe possible implementation of the three-value logic circuits based on the magnonic interferometric switches. The advantages and shortcomings inherent in interferometric switches are also discussed. *Published by AIP Publishing.* [<http://dx.doi.org/10.1063/1.4973115>]

I. INTRODUCTION

Spintronics has been recognized as a new emerging approach towards novel computing devices, which takes advantages of spin in addition to the electric charge.¹ The electron wave analog of the electro-optic light modulator proposed by Datta and Das is one of the best known examples.² The schematics of the modulator and its output characteristics are shown in Fig. 1(a). This is a three-terminal electronic device with the source, drain, and gate contacts, where the source-to-drain current is controlled by the application of the gate voltage. On the first look, this device is very similar to an ordinary semiconductor field effect transistor (FET). However, its principle of operation is completely different. The source and the drain are made of a ferromagnetic (or half-metallic) material working as the polarizer and analyzer for the spin polarized current. The electrons are injected into a quasi-one-dimensional semiconductor channel from the magnetic source. The probability that the electrons will be transmitted through the channel/drain interface depends on the relative orientation of the electron's spin with the drain magnetization. The precession of the injected spins in the channel is controlled with a gate potential via the Rashba spin-orbit coupling effect. Thus, the source-drain current oscillates as a function of the gate voltage similar to the intensity modulation in the electro-optic modulators.² This work² has stimulated a great deal of research in the field of spintronics. The first working spin-FET prototype based on the InAs heterostructure was demonstrated in 2009.³ This

device shows an oscillatory conductance as a function of the applied voltage as was originally predicted by Datta and Das.²

The lack of efficient spin injection and short spin diffusion length in the channel are the two major problems inherent to all spin-FETs. Being injected into a semiconductor channel, the spins of conduction electrons are subject to different relaxation mechanisms (e.g., Elliott–Yafet,⁴ D'yakonov and Perel',⁵ and Bir *et al.*⁶), which reduce the spin polarization. All scattering mechanisms tend to equalize the number of spin up and spin down electrons in a non-magnetic semiconductor channel. In turn, the variation of the spin polarization among the ensemble of conducting electrons reduces the On/Off ratio. In the best scenario, materials with the high mobility and low scattering (e.g., graphene) show electron spin diffusion length of the order of several micrometers at room temperature.⁷ The problems associated with limited spin diffusion length can be resolved by utilizing collective spin phenomena, where the interaction among a large number of spins makes the system more immune to the scattering. A spin wave is a collective oscillation of spins in a lattice around the direction of magnetization. Spin waves appear in magnetically ordered structures, and a quantum of spin wave is referred to as a magnon. The collective nature of spin wave phenomena manifests itself in relatively long coherence length, which may be order of the tens of micrometers in conducting ferromagnetic materials (e.g., $Ni_{81}Fe_{19}$ (Ref. 8)) and exceed millimeters in non-conducting ferrites (e.g., $Y_3Fe_2(FeO_4)_3$

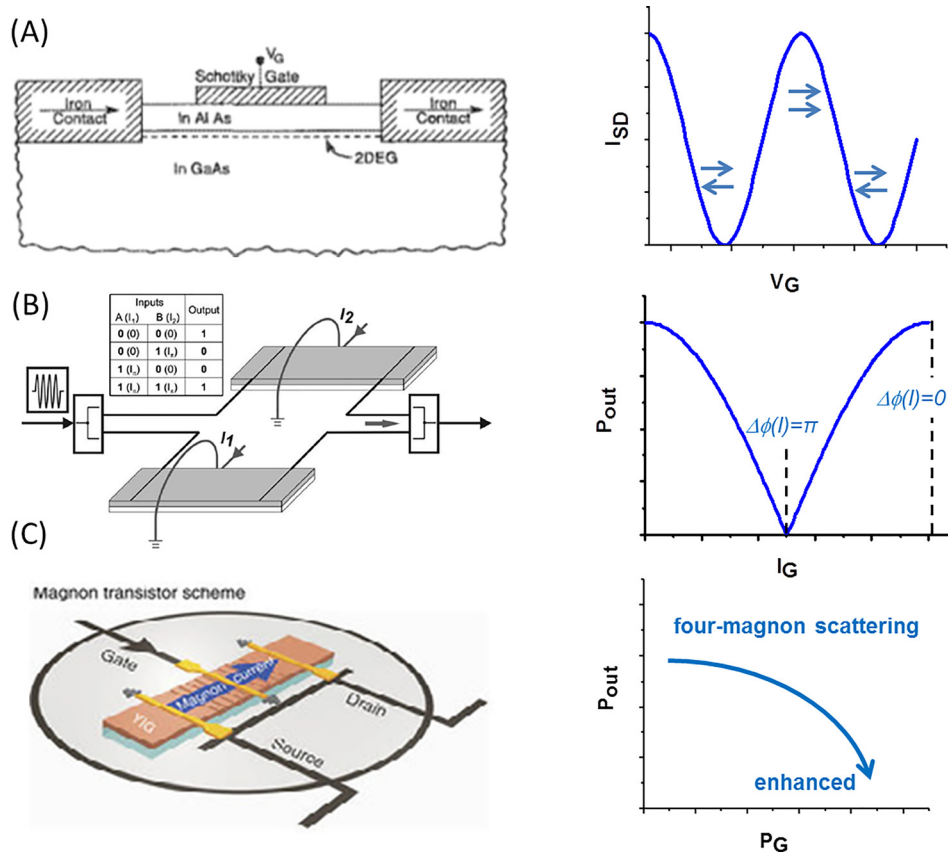


FIG. 1. Schematics and input-output characteristics of selected spin-based switches. (a) Electro-optic modulator proposed by Datta and Das. The flow of the spin polarized electron in the channel is controlled by the gate voltage via the Rashba spin-orbit coupling effect. The source-drain current oscillates as a function of the gate voltage. Reproduced with permission from, Appl. Phys. Lett. **56**(7), 665–667 (1990). Copyright 1990 AIP Publishing LLC. (b) Mach-Zehnder spin wave interferometer. The output inductive voltage is controlled by the phase difference among the interfering spin waves. In turn, the phase difference is controlled by the magnetic field generated by DC electric current in the gate wire. Output inductive voltage oscillates as a function of the gate current. Reproduced with permission from Appl. Phys. Lett. **87**(15), 153501–153503 (2005). Copyright 2005 AIP Publishing LLC. (c) Magnon transistor. The flow of magnons from the source to the drain is modulated by the magnons injected at the gate via the four-magnon scattering. The injection of the gate magnons suppresses the source-drain magnon current. Reproduced with permission from Nat. Commun. **5**, 1–8 (2014). Copyright 2014 AIP Publishing LLC.

(Ref. 9)) at room temperature. The first working spin wave-based logic device was experimentally demonstrated in 2005 by Kostylev *et al.*¹⁰ In this work, the authors built a Mach-Zehnder-type spin wave interferometer to demonstrate the output voltage modulation as a result of spin wave interference. The schematics and the output characteristics of the spin wave device are shown in Fig. 1(b). The phase difference among the spin waves propagating in the arms of the interferometer is controlled by the magnetic field produced by the electric current I_G . At some point, the output characteristics of this device resemble the ones of the Datta and Das device, while the oscillation of the output voltage is controlled by the magnetic field (gate current).

Later on, exclusive-not-OR and not-AND gates have been experimentally demonstrated on a similar Mach-Zehnder-type structure.¹¹ However, the cascading of several of such devices in a circuit requires spin wave-to-magnetic field conversion, which dictates a need in additional converter circuits. This issue has been addressed in the magnon transistor demonstrated by Chumak *et al.* in 2013.¹² The schematics and the output characteristics of the magnon transistor are shown in Fig. 1(c). The transistor is based on a magnonic crystal designed in the form of an yttrium iron garnet (YIG) film with an array of parallel grooves at its surface.

The magnons are injected into the transistor's source and are detected at the drain using microstrip antennas. The magnons that control the source-to-drain magnon current are injected directly into the magnonic crystal (transistor's gate). The principle of operation is based on the nonlinear four-magnon scattering mechanism, which makes it possible to attenuate source-drain transport when gate magnons are injected. The injection of the gate magnons suppresses the source-drain magnon current as illustrated in Fig. 1(c).

In this work, we describe a magnonic switch based on the spin wave interference. We argue that the relatively simple interference-based device possesses output characteristics similar to the Datta and Das device as shown in Fig. 1(a). The proposed device makes it possible to exploit both the phase and amplitude of the output as in the spin wave Mach-Zehnder interferometer shown in Fig. 1(b) and allows one to build all-magnon logic circuits similar to the magnon transistor shown in Fig. 1(c). The rest of the paper is organized as follows. In Section II, we describe the principle of operation of a scaled nanometer size magnonic switch and describe possible multi-valued logic circuits. In Section III, we present experimental data obtained for a micrometer scale prototype based on the YIG structure. Theoretical analysis and results of micromagnetic simulations are given in

Section IV. We also present the results of numerical simulations illustrating the operation of the ultimately scaled switch consisting of two 1-D spin channels. The discussion and conclusions are given in Sections V and VI, respectively.

II. PRINCIPLE OF OPERATION

In order to explain the principle of operation of the magnonic interferometric switch, we start with a theoretical model describing spin wave interference in a nanometer-scale structure. The schematic of the magnonic interferometric switch is shown in Fig. 2(a). It is a three-terminal junction comprising two spin channels. To be consistent with the examples of spin-based devices shown in Fig. 1, we depict the three terminals as a “source,” a “gate,” and a “drain.” The source-drain channel is a one-dimensional chain of spins coupled via the exchange interaction. The gate is connected to the source-drain channel via the one-dimensional chain of spins. These two chains are shown orthogonal to each other in Fig. 2(a) though the angle of the junction is not of critical importance. The input signal coming from the source is a continuous spin wave $m_S(r, t)$ of fixed frequency f , amplitude A_S , and phase φ_S

$$m_S(r, t) = A_S \cdot \exp[-\kappa r] \cdot \sin(k_0 r - \omega t + \varphi_S), \quad (1)$$

where κ is the damping constant, r is the distance traveled, k_0 is the wave vector, $\omega = 2\pi f$, and t is the time. The control signal is also a continuous spin wave of the same frequency f , amplitude A_G , and phase φ_G . These two waves propagate through the spin chains and reach the drain. The output of

the device is a spin wave—a result of the spin wave interference

$$m_D(r, t) = m_S(r, t) + m_G(r, t). \quad (2)$$

The amplitude A_D and phase φ_D of the output depend on the phase difference between the interfering waves $\Delta\varphi_{SG} = (\varphi_S - \varphi_G)$. The output has maximum amplitude if the spin waves are coming in phase (constructive interference = On state). The output has minimum amplitude if the waves are coming out of phase (destructive interference = Off state). In Fig. 2(b), we depicted the amplitude of the output A_D as a function of the source-gate phase difference $\Delta\varphi_{SG}$ assuming the waves reach to the drain with the same amplitude (e.g., $A_S = A_G$).

Conventional digital logic circuits operate with a two-valued logic where 0 and 1 correspond to the two levels of voltage or current (i.e., On and Off states of FET). The output characteristics of the magnonic interferometric switch are also suitable for amplitude encoding, where On and Off states correspond to the cases of constructive and destructive interference. In theory, the On/Off ratio of the magnonic switch is infinity, as there is zero amplitude output in the case of the destructive interference. In practice, the On/Off ratio is limited by the thermal noise level as will be discussed later in the text. In addition to the amplitude, we can also utilize the phase of the output as a logic variable. For example, there may be several On states with the same amplitude but different phase φ_D (e.g., 0 or π). The benefit of having phase in addition to amplitude can be utilized for multi-valued logic.¹³

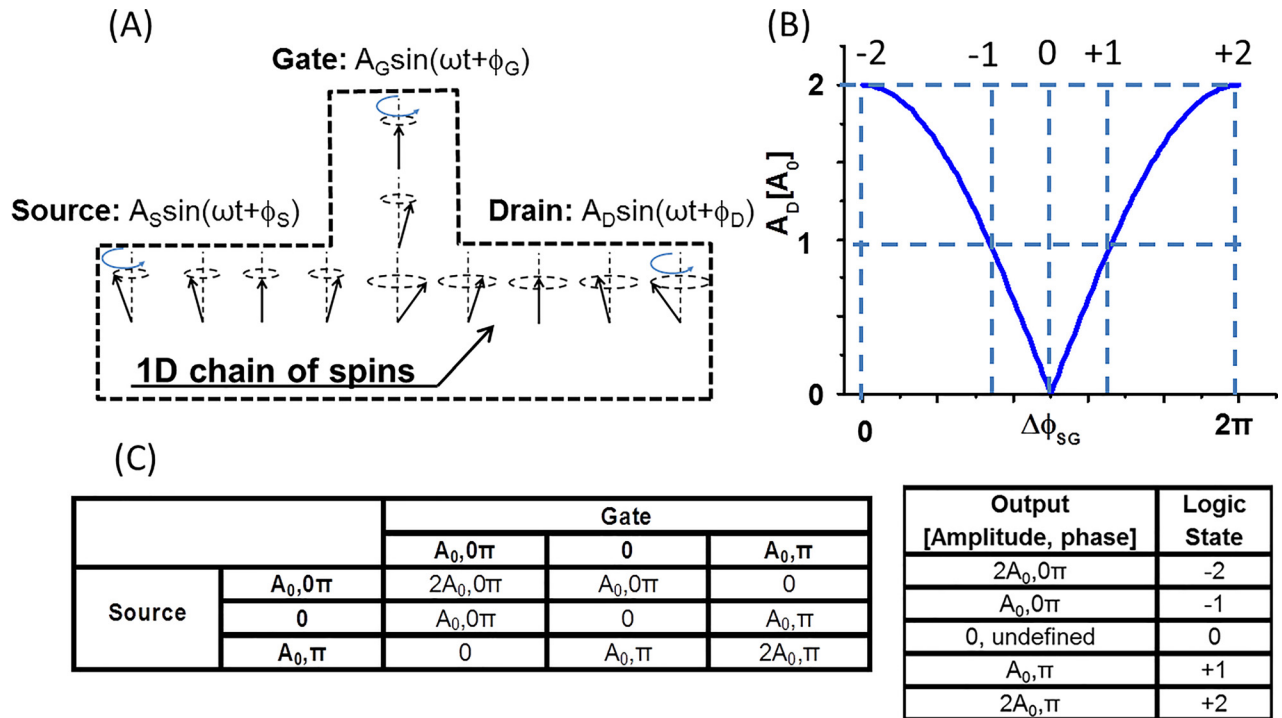


FIG. 2. (a) Schematics of the magnonic interferometric switch. It is a three-terminal junction comprising the two lines of spin channels. The source, the gate, and the drain terminals are depicted by letters S, G, and D. One of the spin chains serves as a source-drain channel, and the other chain connects the gate with the source-drain channel. The source and the gate signals are spin waves. (b) Output characteristics of the magnonic switch. The amplitude and the phase of the output spin wave depend on the amplitudes and phases of the source and gate spin waves. The Table below the output characteristics shows 5 selected output states to be used for multi-valued logic gate construction. (c) Truth Tables illustrating the logic operation of the magnonic interferometric switch.

In order to illustrate this idea, we choose five output states as depicted in Fig. 2(c): $[-2$ logic state: $A_D = 2A_0$, $\varphi_D = 0\pi$]; $[-1$ logic state: $A_D = A_0$, $\varphi_D = 0\pi$]; $[0$ logic state: $A_D = 0$, φ_D is not defined]; $[+1$ logic state: $A_D = A_0$, $\varphi_D = \pi$]; $[+2$ logic state: $A_D = 2A_0$, $\varphi_D = \pi$]. Sign plus or minus corresponds to the phase of the output (e.g., 0 or π), while the digits correspond to the amplitude of the output: $2A_0$, $1A_0$, or $0A_0$, where A_0 is some reference amplitude). Hereafter, 0 amplitude stands for amplitude below the thermal noise limit. The reason of taking these particular states lies in the specific of interferometric switching. Let us consider the operation of magnonic switch as shown in Fig. 2(a), in the case of only three possible states: -1 , 0 , and $+1$ for the source and the gate. There are 9 possible input state combinations resulting in the 5 possible output states (e.g., -2 , -1 , 0 , $+1$, and $+2$) as summarized in the Table in Fig. 2(c). The application of the 5-states input to the next interferometric switch would result in the 9 possible states for the output (e.g., two possible phases and five possible amplitudes). In this work, we consider an example of the three-valued (3VL) logic gates.¹⁴ There are two more elements required for 3VL logic gate construction, which are a π -phase shifter; and an attenuator as shown in Fig. 4(a). These are two passive non-linear elements for independent phase and amplitude modulation. The π -phase shifter provides a π -phase shift to the propagating spin waves. It may be an additional chain of spins (i.e., similar to the delay lines used in optics¹⁵), or a permanent magnet placed near the chain, or a resonator.¹⁶ The combination of the magnonic interferometric switch and the phase shifter provides the NOT gate (i.e., the truth table in Fig. 3(a)). A π -phase shift is equivalent to the 3VL Inverter logic operation $-1 \rightarrow +1$; $0 \rightarrow 0$; $+1 \rightarrow -1$. The attenuator is also a passive device (e.g., similar to a non-linear resistor in electric circuits), which reduces the

amplitude of the transmitted spin wave signal $2A \rightarrow A$, $A \rightarrow 0$, and $0 \rightarrow 0$. For example, the placement of any conductor near the waveguide introduces additional losses which results in the spin wave damping. The introduction of the attenuator reduces the number of possible output states from 5 to 3. The combination of the attenuator with the magnonic switch makes it possible to realize 3VL XOR gate as depicted in Fig. 3(b). The combination of the NOT and XOR gates allows us to build all other types of logic gates similar to the conventional two-valued Boolean logic.¹⁷ In general, the multi-valued logic devices offer significant advantages over the binary counterparts including a fewer number of components per circuit, more efficient use of interconnects, and lower power dissipation. A comprehensive review on multiple-valued logic can be found in Ref. 18. There were a number of attempts of building multi-state circuits with conventional CMOS.¹⁹ However, the lack of any true multistate device is the main challenge towards the multi-valued logic practical implementation.¹⁸

III. EXPERIMENTAL DATA

In this Section, we present experimental data obtained on a micrometer scale prototype based on the available four-terminal cross junction made of yttrium iron garnet $Y_3Fe_2(FeO_4)_3$. The photo of the device and connection schematics is shown in Figure 4. The cross junction is made of a single crystal YIG film epitaxially grown on top of a Gadolinium Gallium Garnett ($Gd_3Ga_5O_{12}$) substrate using the liquid-phase transition process. After the films were grown, sub-millimeter patterning was performed by laser ablation using a pulsed infrared laser ($\lambda \approx 1.03 \mu m$), with a pulse duration of ~ 256 ns. The YIG cross has the following dimension: the length of the each waveguide L is 3.65 mm;

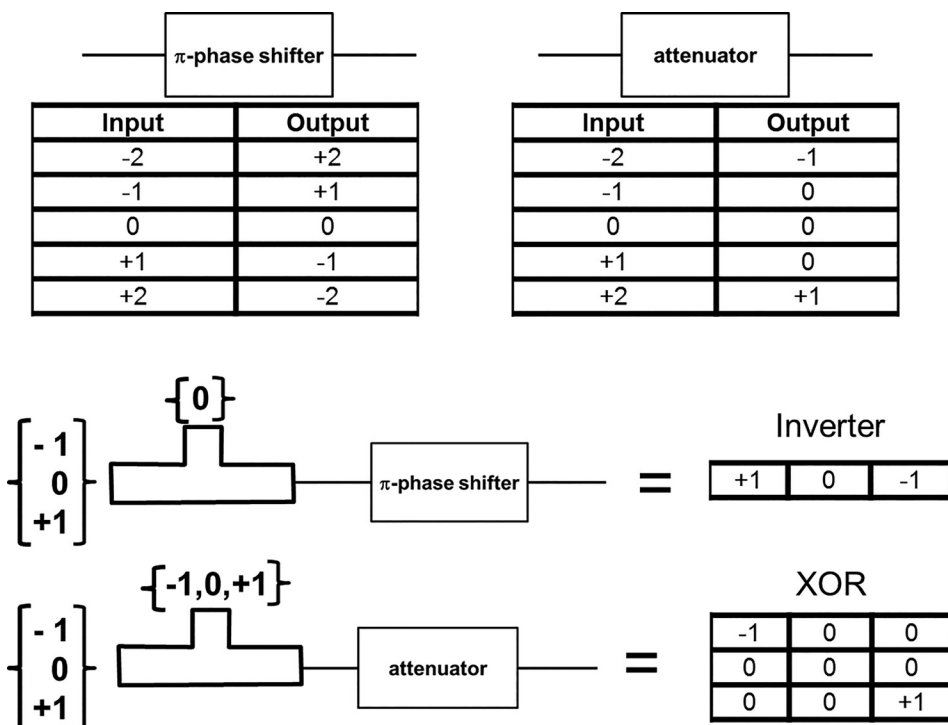


FIG. 3. (a) Symbols and truth tables of the two passive elements for independent phase and amplitude modulation: A- π phase shifter provides an a- π phase shift to the propagating spin wave, and an attenuator introduces an exponential damping to the propagating spin wave. (b) Schematics of the NOT and XOR 3VL gates built of the magnonic interferometric switch and the passive elements.

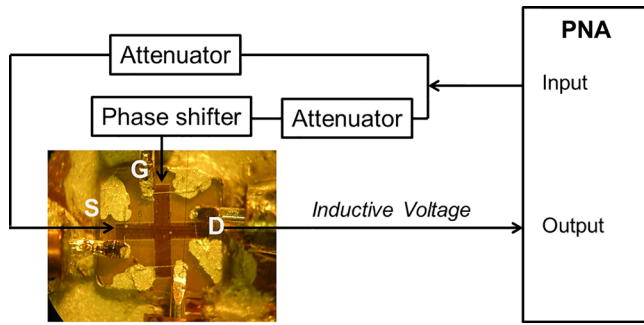


FIG. 4. Photo of the YIG cross junction and connection schematics. The length of the cross is 3 mm; the width is $360\ \mu\text{m}$; and the YIG film thickness is $2.0\ \mu\text{m}$. There are four Π -shaped micro-antennas fabricated on the edges of the cross. Antennas are connected to a programmable network analyzer (PNA) Keysight N5241A. Two continuous spin wave signals are excited at terminals S and G. The inductive voltage is detected at terminal D. There are attenuators and a phase shifter aimed to equalize the amplitudes of the input waves and control the phase difference between the S and G terminals.

the width w is $650\ \mu\text{m}$; the YIG film thickness d is $3.8\ \mu\text{m}$; and saturation magnetization of $4\pi M_0 \approx 1750\ \text{Oe}$, and ferromagnetic resonance (FMR) linewidth $\Delta H \approx 0.5\ \text{Oe}$. There are four Π -shaped micro-antennas fabricated on the edges of the cross. Antennas were fabricated from a gold wire of thickness $24.5\ \mu\text{m}$ and placed directly on the top of YIG surface. The antennas are connected to a programmable network analyzer (PNA) Keysight N5241A. Two of the antennas depicted by the letters S and G are used to generate the “source” and the “gate” spin waves, respectively. The inductive voltage is detected by the “drain” antenna as depicted in Fig. 4. Spin waves were excited by the magnetic field generated from the AC electric current flowing through the S and G antennas. We used a set of attenuators (PE7087) and a phase shifter (ARRA 9428A) to independently control the power and the phase difference between the input signals. The inductive voltage produced by the interfering spin waves was detected by the drain antenna D. The details of the inductive measurement technique can be found elsewhere.²⁰ In our experiments, we used the attenuator and the amplifier depicted in Fig. 4 to equalize the output voltages produced by the S and G antennas operating separately.

We carried out three sets of experiments aimed to show the output inductive voltage modulation by the phase difference between the source and the gate spin waves. The experiments were accomplished at three different directions of the bias magnetic field. The direction of the bias magnetic field significantly affects the dispersion of the propagating spin waves. For instance, magnetostatic spin waves propagating parallel to the bias magnetic field (so-called backward volume magnetostatic spin waves BVMSW) possess negative group velocity $v_g = \partial\omega/\partial k < 0$, while spin waves propagating perpendicular to the bias magnetic field (so-called magnetostatic surface spin waves MSSW) possess positive group velocity $v_g > 0$.²¹ It is critically important for the operation of the cross-type magnonic devices to ensure the propagation of the both types of waves. The latter is possible by finding a proper combination of the operational frequency and the bias magnetic field. Prior to the experiments, we found such a combination corresponding to the operational

frequency $f = 4.095\ \text{GHz}$ and bias magnetic field $H = 798\ \text{Oe}$. All experiments are done at room temperature.

In Fig. 5(a), we present experimental data for the bias magnetic field H directed parallel to the virtual S-D line. In this case, there is a BVMSW type of spin wave propagating from the source to the drain, and a MSSW type of spin wave propagating from the gate to the S-D channel. The input power of the S-antenna was set to $-24\ \text{dBm}$, and the power of the G-antenna was set to $-6\ \text{dBm}$. The red and blue markers show the amplitude and the phase of the output voltage as a function of the phase difference between the S and G antennas $\Delta\varphi_{SG}$. We collected experimental data for 22 points with different $\Delta\varphi_{SG}$ in the range from 0 to 2π . The accuracy of the phase detection by PNA is 0.008π . There are two maxima about $0.414\ \text{mV}$ corresponding to the constructive spin wave interference (i.e., the inductive voltage produced by only S operating antenna is $0.225\ \text{mV}$, and the inductive voltage produced by only G operating antenna is $0.219\ \text{mV}$). The minimum voltage corresponding to the destructive spin wave interference is about $0.01\ \text{mV}$. The accuracy of the inductive voltage measurements at minima is $\pm 0.00046\ \text{mV}$. The red curve in Fig. 5(a) shows the results of numerical modeling in the ideal case where S and G spin waves have zero phase/amplitude variation. The blue markers in Fig. 5(a) depict the measured phase of the output signal. The phase of the output φ_D is defined with respect to the phase of the S input (i.e., $\varphi_D = \Delta\varphi_{DS}$). The phase difference between the input and the output spin waves can be described as a sum of two

$$\Delta\varphi_{DS} = \Delta\varphi_r + \Delta\varphi_{int}, \quad (3)$$

where $\Delta\varphi_r$ is the phase accumulated during the spin wave propagation (i.e., $\Delta\varphi_r = kr$), and $\Delta\varphi_{int}$ is the phase change as a result of the interference with the gate wave (if the gate wave has a non-zero amplitude). The first term in Eq. (3) does not depend on the input phases of the waves generated at the S and G terminals. It explains the phase difference between the source and the output waves in the case of constructive interference. The second term is responsible for the output phase oscillation $\pm\pi/2$. The jump of the output phase within the region of the destructive interference is the clear indication of the interference $\Delta\varphi_{int}$.

Next, we carried out similar experiments for the bias magnetic field H directed in-plane but perpendicular to the virtual S-D line. In this case, there is a MSSW type of spin wave propagating from the source to the drain and a BVMSW type of spin wave propagating from the gate to the S-D channel. The input power of the S-antenna is $-18\ \text{dBm}$ and the power of the G-antenna is $-12\ \text{dBm}$. As in the previous example, we measured the inductive voltage as a function of the phase difference between the source and the gate antennas. The red markers and the red curve in Fig. 5(b) show experimental data and the results of numerical modeling, respectively. The blue markers and the blue curve in Fig. 5(b) correspond to the experimentally measured and calculated phase of the output. The amplitude of the inductive voltage has maxima about $0.448\ \text{mV}$, while the minimum output inductive voltage below $0.02\ \text{mV}$.

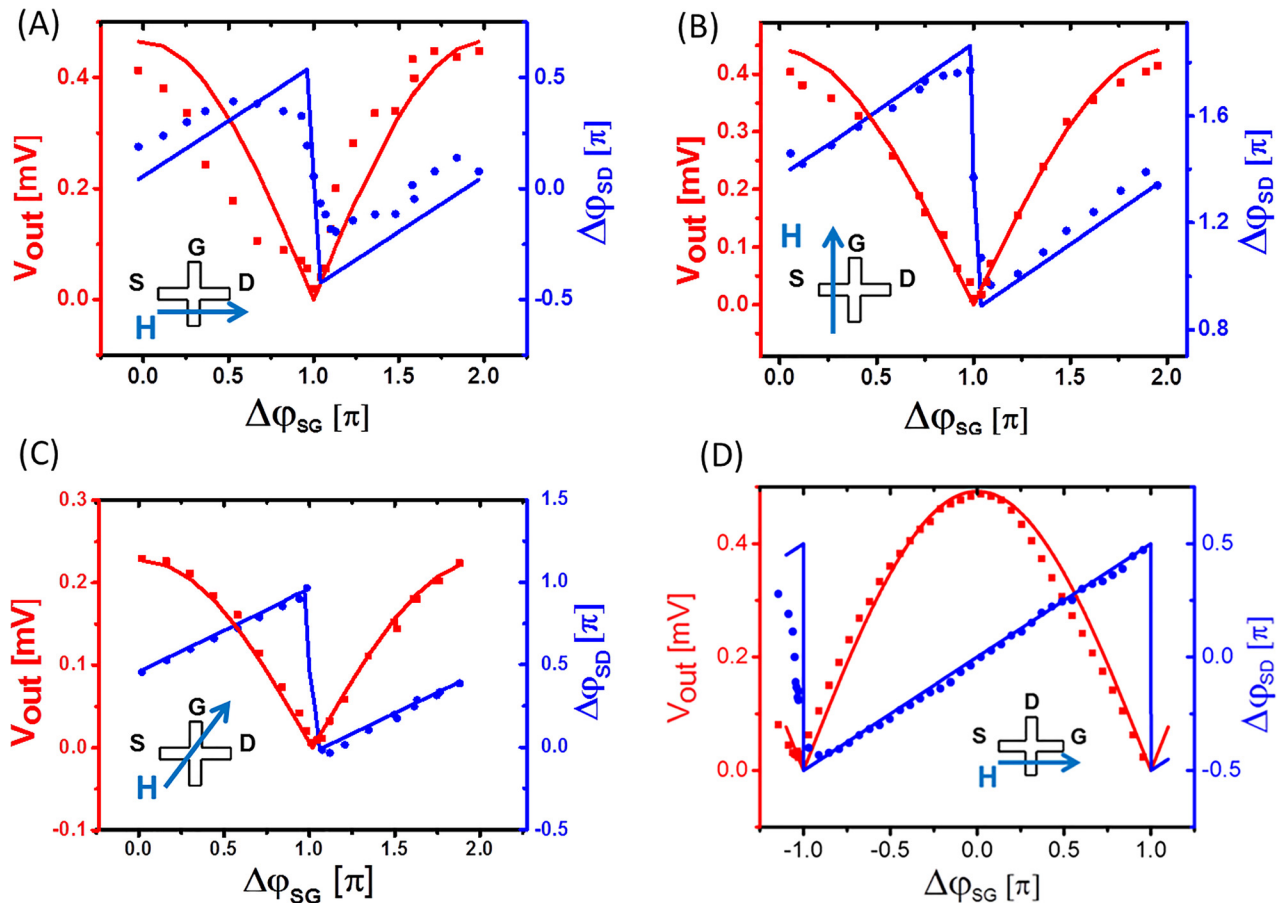


FIG. 5. Experimental data demonstrating output voltage modulation by the phase difference between the S and G terminals. The operational frequency is 4.095 GHz, and bias magnetic field $H = 798$ Oe. The red markers show experimentally measured output voltage. The red curve shows output voltage calculated in the ideal case of zero input phase/amplitude variation. The blue markers depict the phase of the output. The output phase is defined with respect to the phase of the spin wave generated at the terminal S. (a) Bias magnetic field is directed along the virtual S-D line. (b) Bias magnetic field is directed perpendicular to the virtual S-D line. (c) Bias magnetic field is directed at 45° to the virtual S-D line. (d) Results for modified configuration, where the source and the gate antennas are located on the same arm of the cross as shown in the inset. The bias magnetic field H is directed parallel to the virtual S-G line.

Then, we carried out experiment with the bias magnetic field H directed in-plane and at 45° to the virtual S-D line. Experimental data and the results of numerical modeling are presented in Fig. 5(c). The input power of the S-antenna was set to -30 dBm, and the power of the G-antenna was set to -9 dBm. The red and blue markers in Fig. 5(c) show the amplitude and the phase of the output voltage. The maximum output inductive voltage is 0.227 mV, (i.e., the inductive voltage produced by only S operating antenna is 0.114 mV and the inductive voltage produced by only G operating antenna is 0.117 mV).

Finally, we carried out experiment in the configuration where the source and the gate antennas are located on the same arm of the cross, while the inductive voltage is measured at the orthogonal arm. This configuration is shown in the inset to Fig. 5(d). The bias magnetic field H is directed parallel to the virtual S-G line. The operational frequency was decreased to 3.442 GHz. Experimental data and the results of numerical modeling are presented in Fig. 5(d). The input power of the S-antenna and the G-antenna was set to -13 dBm. The red and blue markers in Fig. 5(d) show the amplitude and the phase of the output voltage. The maximum output inductive voltage is about 0.49 mV, while the On/Off ratio is 22 dB.

Experimental data presented in Figs. 5(a)–5(d) demonstrate prominent output voltage modulation by the phase difference among the source and the gate signals $\Delta\phi_{SG}$. This output characteristic is well explained by the spin wave interference. As one can see from Figs. 5(b), 5(c), and 5(d), there is a good agreement between the experimental and theoretical data. The observed discrepancy in Fig. 5(a) is mainly due to the variation of the input amplitude and phases of the input spin waves. The maximum voltage is observed in the case of constructive spin wave interference $\Delta\phi_{SG} = 0$, where the amplitude of the output doubles compared to the output produced by just on operating antenna. The major discrepancy between the theoretical and experimental data is observed for $\Delta\phi_{SG} = \pi$, which corresponds to the destructive interference between the source and the gate waves. The results of numerical modeling show zero output amplitude, while the experimental data show some finite amplitude. The On/Off ratios calculated from experimental data show: 27 dB in Fig. 5(a), 32.1 dB in Fig. 5(b), 36.1 dB for the 45° geometry shown in Fig. 5(c), and 22 dB for the geometry with source and drain located on the same arm in Fig. 5(d). The discrepancy between the experiment and theoretical data may be attributed to many factors including structure imperfections, amplitude, and phase variation of the input waves.

Thermal noise is the major and fundamental factor limiting the On/Off ratio of the interferometric switch. The dephasing and damping of spin waves caused to the magnon-phonon and other scattering processes will result in a non-zero output.

Every new proposed switch and logic circuit should demonstrate certain noise immunity to be useful for practical applications.^{22,23} There are numerous internal and external noise sources, which can affect the circuit performance. New device designs and material systems used in their implementation require investigation of dominant noise mechanisms and methods for noise level reduction.^{24–26} The reported data on noise in magnonic type devices are limited.^{27,28} In this work, in order to study the effect of noise on the device functionality, we collected data for 15 000 subsequent measurements (150 points per 448 ms sweep), which show the output voltage variation at fixed input parameters. In Fig. 6, we present raw data collected for the configuration with the bias magnetic field H directed perpendicular to the virtual S-D line (i.e., as shown in Fig. 5(b)). The sampling rate is 334 Hz. The signal was represented as $\Delta V(t) = V(t) - V_m$, where $V(t)$ is the recorded signal and V_m is the mean value of output voltage. The red and blue markers in Fig. 6 correspond to constructive and destructive cases, respectively. There is about 2 dB variation of the On state, while there is more than 30 dB variation of the Off state. There is a 13 dB gap between the red and blue markers for all 15 000 measurements. We conservatively take it as the On/Off ratio, though the maximum value (e.g., data shown in Fig. 5(a)) exceeds 30 dB. The noise power spectral density of the output was obtained by performing FFT on $\Delta V(t)$. The extracted normalized noise spectral density, S_V/V^2 , was around 10^{-11} 1/Hz at 1 Hz. This noise level is higher than the thermal noise floor defined by the Nyquist formula $S_V = 4k_B TR$ (where k_B is the Boltzmann constant, T is the absolute temperature, and R is the resistance) but comparable to the noise level in conventional Si CMOS devices. The low noise spectral density $S_V/V^2 \sim 10^{-11}$ 1/Hz achieved in the prototype devices (not optimized for noise reduction)

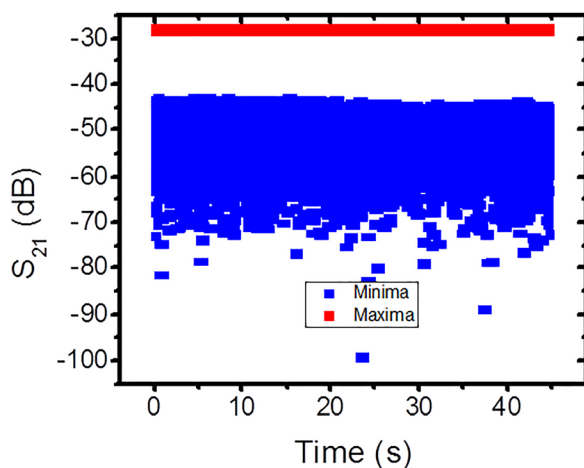


FIG. 6. Experimental data for 15 000 subsequent measurements (150 points per 448 ms sweep) showing the variation of the output voltage in time at fixed input parameters. The markers depict the maximum output voltage measured for the On state (i.e., constructive interference). The blue markers show the variation of the output voltage for the Off state (destructive interference).

suggests a possibility of extremely low-noise designs achievable with the proposed magnonic interferometric switch.

IV. THEORETICAL ANALYSIS AND NUMERICAL MODELING

Experimental data presented in Sec. III show significant difference in the device output characteristics depending on the direction of the bias magnetic field. Potentially, this effect may be utilized for building re-configurable magnetic-magnonic logic circuits.²⁹ The understanding of the mechanism of spin wave transport in cross-shape junctions is the key to the device optimization. As we mentioned before, spin waves excited at the source and the gate possess different dispersion (i.e., BVMSW and MSSW). In order to provide maximum spin wave transport through the junction, one has to find the region in the bias magnetic field—operational frequency space, where the both types of waves can propagate.

In the case of infinite and uniformly magnetized films, BVMSW and MSSW have non-overlapping frequency ranges $[\omega_H, \omega_0]$ and $[\omega_0, \omega_S]$, respectively, where $\omega_H = \gamma H$, $\omega_0 = \sqrt{\omega_H(\omega_H + \omega_m)}$, $\omega_m = \gamma 4\pi M_0$, $\omega_S = \omega_H + \omega_m/2$, ($\omega_H < \omega_0 < \omega_S$), and γ is the gyromagnetic ratio. The experimentally observed coupling may be explained by taking into consideration the effect of the magnetic field anisotropy caused by the demagnetization fields in the cross junction. In order to estimate the width of the overlap region, we present estimates based on the formalism developed for a homogeneously magnetized ellipsoid.²¹ The demagnetization field can be related to the magnetization of the sample by

$$\vec{H}^m(\vec{r}) = -\hat{N}(\vec{r})\vec{M}(\vec{r}), \quad (4)$$

where $\hat{N}(\vec{r})$ is the tensor of demagnetization coefficients, which has a diagonal form for the main axes of homogeneously magnetized ellipsoid $\sum_i N_{ii} = 1$. Neglecting the non-uniformity of $\vec{M}(\vec{r})$, the frequency of the ferromagnetic resonance ω_0 in the waveguides is given as follows:²¹

$$\omega_0 = \sqrt{[\omega_H + (N_{11} - N_{33})\omega_m] \cdot [\omega_H + (N_{22} - N_{33})\omega_m]}, \quad (5)$$

where the external magnetic field H is directed along the \vec{e}_3 axis of the ellipsoid. The demagnetization factors depend on the structure geometry. For instance, the experimental data presented in the previous section are obtained for the cross structure with $L \gg w \gg d$, where L is the length, w is the width, and d is the thickness of the YIG cross. In this case, one may restrict consideration by the width- N_d and thickness-related N_w demagnetization fields as $N_d \gg N_w \gg N_L$.

Then, for the case shown in Figure 5(a), the long-wavelength limit (i.e., FMR frequency) of the spin waves generated by the source can be found as follows:

$$\begin{aligned} \omega_0^S &= \sqrt{[\omega_H + (1 - N_w)\omega_m] \cdot [\omega_H + N_w\omega_m]} \\ &= \sqrt{\omega_0^2 + N_w \cdot (1 - N_w)\omega_H\omega_m}. \end{aligned} \quad (6)$$

At the same time, the long-wavelength limit for the spin wave generated at the gate is given by

$$\begin{aligned}\omega_0^G &= \sqrt{[\omega_H + (1 - 2N_w)\omega_m] \cdot [\omega_H - N_w\omega_m]} \\ &= \sqrt{\omega_0^2 - N_w \cdot \omega_m(3\omega_H + 2N_w\omega_m)}.\end{aligned}\quad (7)$$

Eqs. (6) and (7) reveal the difference in the effect of the demagnetization field N_w on the FMR frequency ω_0 . The appearance of the demagnetization field may increase ω_0^S while decreasing ω_0^G . The value of the demagnetization field can be estimated by using the on-line calculator,³⁰ which gives $N_w = 0.012$ for the given YIG cross geometry. Then, we estimate the overlap frequency region $\Delta\omega_0^{S,G} = \omega_0^S - \omega_0^G$ for the spin wave generated by the S and G antennas (i.e., BVMSW and MSSW, respectively) as follows:

$$\Delta\omega_0^{S,G} \approx \frac{2N_w\omega_H\omega_m}{\omega_0}.\quad (8)$$

The width of the overlap region $\Delta\omega_0^{S,G}$ for the YIG cross with given geometry at the bias magnetic field $H = 1$ kOe is about $\Delta f = \Delta\omega_0^{S,G}/2\pi \approx 70$ MHz. The FMR frequencies can be also estimated using OOMMF,³¹ which gives $\omega_0^S/2\pi \approx 4.657$ GHz and $\omega_0^G/2\pi \approx 4.595$ GHz ($\Delta f \approx 62$ MHz). These estimates show the possibility of the frequency range overlap and provide an insight into the operational frequency range for a given structure and at certain bias magnetic field.

Figure 7 shows the results of micromagnetic simulations on propagating spin waves in a YIG cross. The direction of the bias magnetic field is the same as in Fig. 5(b). The red arrow in each plot shows the direction of the input spin wave signal. The results show spin wave propagation for three frequencies: 4.50 GHz, 4.64 GHz, and 4.70 GHz, respectively. Two of these frequencies (i.e., 4.50 GHz and 4.70 GHz) are outside the overlap region $\omega_0^S > 2\pi f$ and $2\pi f > \omega_0^G$. Frequency 4.64 GHz is within the overlap region $\omega_0^G > 2\pi f > \omega_0^S$. As one can see

from Fig. 7, the amplitude of the transmitted signal is much higher for the case when the operation frequency is within the overlap region. The maximum spin wave propagation is observed at the frequency close to the FMR of an infinite YIG film $\omega_0/2\pi \approx 4.64$ GHz. It should be also noted the characteristic features of spatial amplitude distribution, which can be attributed to the effect of spin wave quantization as well as to the anisotropy of the spin waves propagating at an angle to the bias field.³²

Scaling down the size of the switch and decreasing the operation wavelength significantly change the spin wave transport. The dispersion of sufficiently short (i.e., shorter than 100 nm) wavelength spin waves (so-called exchange spin waves) differs significantly from the one of the magnetostatic waves.³³ In order to illustrate the operation of a nanometer-scale magnonic interferometric switch, we present the results of numerical simulations. We consider the two perpendicular chains of spins as shown in Fig. 2(a). There are 20 spins in the chain connecting the source and the drain. There are 10 spins in the chain connecting gate and the source-drain channels. In our case, two chains intersect in just one point—one spin. The edge spins at the source and at the gate oscillate with the same frequency f and amplitude A_0 . The neighboring spins in the magnetic wires are coupled via exchange interaction, so the Hamiltonian of the system has the following form:³⁴

$$H = -J \sum_{j\delta} S_j S_{j+\delta} - 2\mu H_0 \sum_j S_{jz},\quad (9)$$

where J is the exchange coupling constant with the dimension of energy, S_j and $S_{j+\delta}$ are the electron-spin operators, S_{jz} is the spin projection along the z direction, the index δ runs over nearest neighbors of spin j , μ is the magnetic moment,

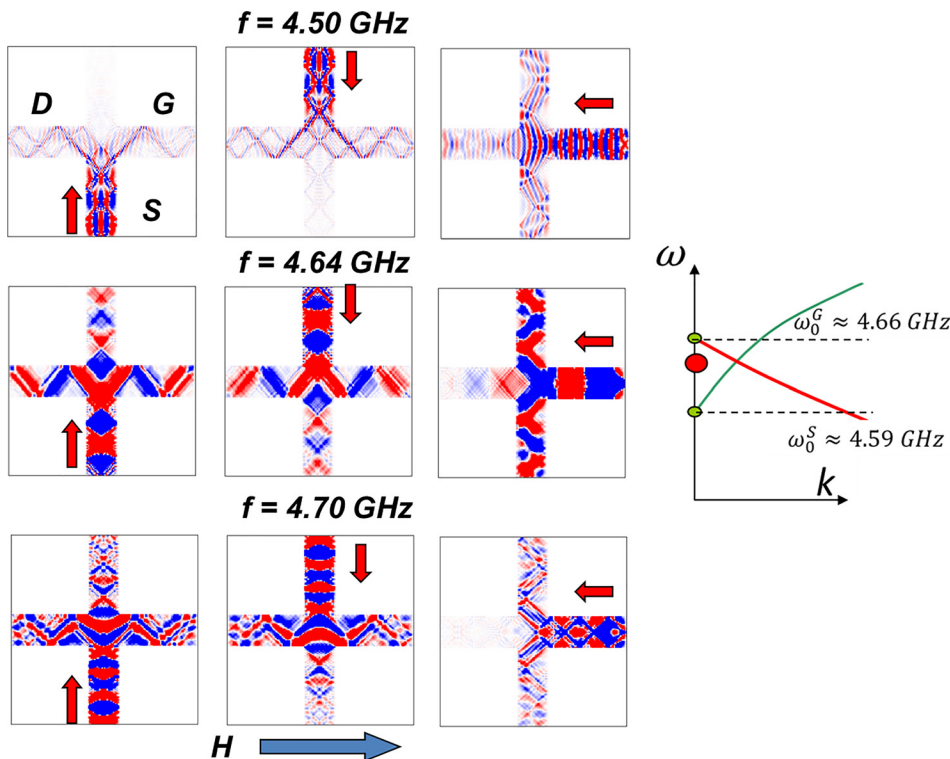


FIG. 7. Results of micromagnetic simulations showing the propagation of spin waves in YIG cross at different operational frequency f . The direction of the bias magnetic field is the same as in Fig. 5(b). The red arrow in each plot shows the direction of the input spin wave signal. (a) Data obtained for $f = 4.50$ GHz. (b) Data obtained for $f = 4.64$ GHz. (c) Data obtained for $f = 4.70$ GHz.

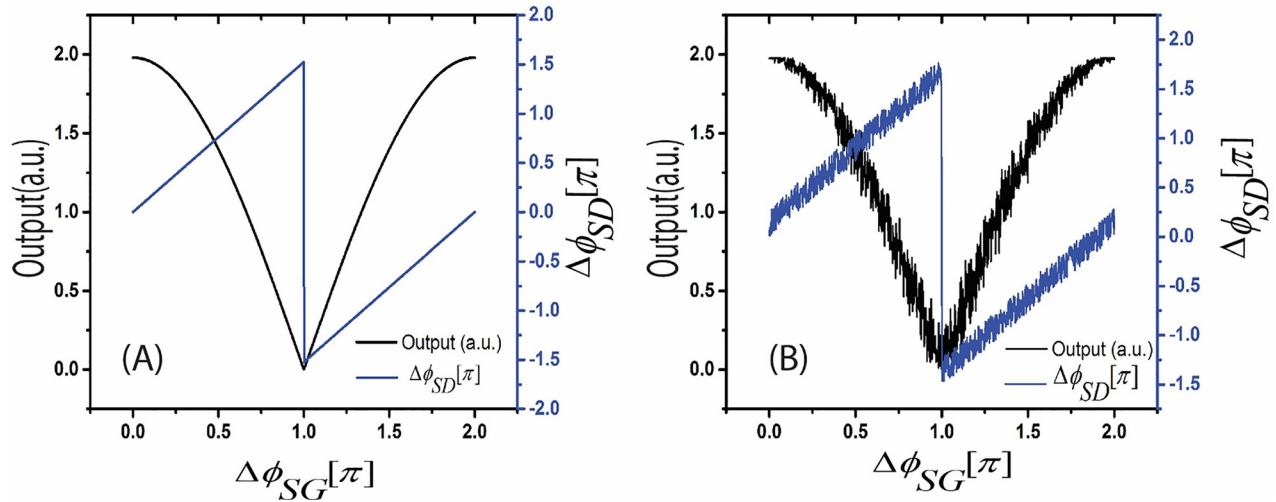


FIG. 8. Results of numerical modeling for nanometer-size switch with just 20 spins in the source-drain channel. The black curve depicts the amplitude of the output spin wave. The blue curve shows the phase of the amplitude. (a) Numerical simulation at zero temperature. (b) Numerical simulations at room temperature.

and H_0 is the external magnetic field strength. The evolution equation for spin j takes the following form:

$$\hbar \frac{d\vec{S}_j}{dt} = \vec{\mu} \times \vec{B}_j, \quad (10)$$

where B_j is the effective magnetic field induction acting on spin j , which arises from the sum of the exchange field due to the coupling with the nearest neighbor spins. The detailed explanations on the one-dimensional chain model can be found elsewhere.³⁴ In Fig. 8, we present the results of numerical modeling showing the amplitude and the phase of the output spin wave depending on $\Delta\phi_{SG}$. The value of the exchange constant J is 70 meV.³⁵ The plot in Fig. 8(a) shows the results of numerical modeling at zero temperature. In this ideal case, the amplitude of the transmitted is $2A_0$ in the case of the constructive interference and zero in the case of the destructive interference (i.e., On/Off ratio is infinity). The plot in Fig. 8(b) shows the results of similar simulations at room temperature (300 K). The effect of the temperature has been included in the simulation through the stochastic Landau-Lifshitz-Gilbert (LLG) equation where the effect of the thermal fluctuations at finite temperature T is characterized by a random field in the LLG equation, and the fluctuation dissipation theorem^{36,37} is satisfied to eventually achieve thermal equilibrium. The stochastic term in the Langevin equation takes into account the effect of finite temperature in the stochastic LLG. The ratio $J/k_B T$ is almost equal to 3, so the temperature acts like a noise field in the simulation which is generated using a random number generator with the mean square value controlled by the temperature in accordance with the Brown's scheme of the Langevin equation. The immediate result of thermal noise is a nonzero output in the case of destructive interference, and in turn, the reduction of the On/Off ratio. In general, the effect of the finite temperature on the output characteristics exponentially increases with the ratio $k_B T/J$. In Fig. 9, we present the results of numerical modeling showing the noise strength as a function of the exchange coupling energy. We subtract

the noisy signal at finite temperature from the signal at zero temperature, take the square of that quantity, and average for different source to gate input signals with different phase shifts to estimate the noise strength for a fixed temperature and exchange coupling. The effect of the thermal noise is less for stronger exchange coupling.

V. DISCUSSION

Spin-wave logic devices have been proposed as a possible alternative to conventional digital logic.³⁸ The utilization of phase in addition to amplitude and compatibility with conventional magnetic memory are the two major advantages of this approach.^{39,40} A natural way of exploiting phase for data processing is by implementing interference-based devices (e.g., as it was demonstrated by Kostylev *et al.* in a Mach-Zehnder-type spin wave interferometer¹⁰). There may be more than two interfering spin waves, which increases the functionality of logic devices. The first three-input MAJ logic prototype based on $\text{Ni}_{81}\text{Fe}_{19}$ has been experimentally demonstrated in 2009.⁴¹ Recently, it has been a growing

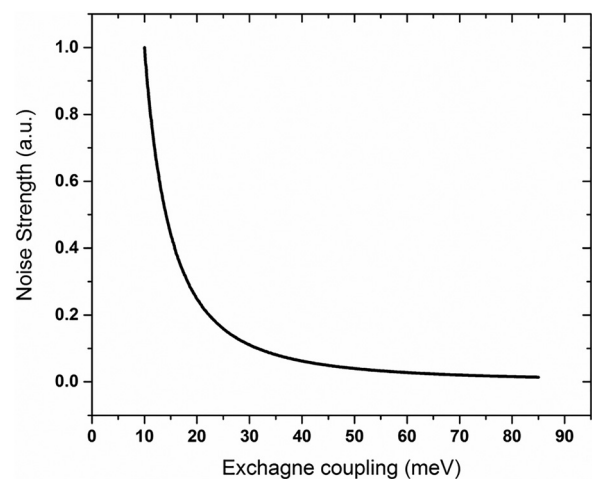


FIG. 9. Results of numerical modeling for the nanometer-size switch showing the noise strength as a function of the exchange coupling energy J .

interest to interference-based magnonic logic devices.^{42–45} In most of the above cited works, there is the same type of interfering spin waves (e.g., MSSW or BVSW) propagating through a waveguide in the same or opposite directions. Any non-uniformity in the waveguide geometry may lead to a significant modification in the spin wave dispersion (see, for example, analysis in Ref. 46). The situation is ever complicated in a cross junction where the two different types of spin-waves meet in the center of the structure. The wave propagating in the two orthogonal arms possesses different group velocities, which, in turn, results in different signal attenuation. We adjusted the input power at the S and G excitation antennas to equalize the amplitudes of the interfering spin waves. For instance, the experimental data presented in Figs. 5(a)–5(c) are achieved at a higher power applied to the G input. The same input power was used for the case shown in Fig. 5(d).

Another important question is related to the non-linear effects (e.g., three- and four-magnon scattering), which may affect spin wave transport. In order to minimize non-linear processes, we kept the input power below the 4-magnon parametric instability threshold. The maximum input power did not exceed -6 dBm (0.25 mW). The level of the input power was chosen at least 10 dBm below than the four-magnon parametric instability threshold for the studied structure. Typically, only 10% of the input power is converted into the spin waves. Thus, the maximum spin wave power P_{msw} in the YIG film does not exceed $25 \mu\text{W}$. The power can be related to the spin wave amplitude as follows:

$$P_{\text{msw}} = |m|^2 v d w, \quad (11)$$

where v is the group velocity, $d = 3.8 \mu\text{m}$, $w = 650 \mu\text{m}$, and $|m|$ is the spin wave amplitude. In turn, the amplitude is related to the angle of the magnetization precession cone φ

$$|m| = \varphi \cdot M_S. \quad (12)$$

Eqs. (11) and (12) allow us to estimate the maximum angle of the magnetization precession

$$\varphi = \sqrt{\frac{P_{\text{msw}}}{M_S^2 v d w}}. \quad (13)$$

Taking the group velocity $v = 4 \times 10^6 \text{ cm/s}$, the maximum angle of precession value $\varphi_{\text{max}} \leq 0.009$. This value is two times less than the threshold value φ_{th} of the 4-magnon parametric instability, which can be estimated as follows:²¹

$$\varphi_{\text{th}} \approx \sqrt{\frac{\Delta H}{4\pi M}}. \quad (14)$$

At this moment, the interaction between MSSW and BVMSW in cross junctions is mainly unexplored and requires further experimental and theoretical study.

There are some unique advantages and shortcoming inherent in magnonic interferometric switch we want to outline. Scalability is the most appealing advantage provided by the utilization of spin waves as the logic variable. In general,

an interferometric switch can be realized on any type of waves (e.g., optical, acoustic, and gravitational). In any case, the minimum feature size of the logic circuit is restricted by the operational wavelength λ (i.e., the minimum size of the inverter shown in Fig. 3 is $\lambda/2$). Spin-wave offers a route toward the nanometer operational wavelength. There are no fundamental physical limits restricting the scaling down the area of the magnonic switch to several square nanometers, while the practically achievable size is limited only by the capabilities of the manufacturing technique. In turn, the time delay τ scales proportional to the length of the structure (e.g., $\tau = L/v_g$, where L is the length of the channel and v_g is the spin wave group velocity). For example, the time delay of the switch with 10 nm long S-D and G-D would be 1 ps conservatively taking $v_g = 10^4 \text{ m/s}$. Low energy consumption is another advantage of the proposed switch. The principle of operation of the magnonic interferometric switch is based on the spin wave interference, where On and Off states correspond to the constructive and destructive interference, respectively. In this approach, there is no fundamental limit on the minimum energy of the interfering waves except the thermal noise. Potentially, the energy of the input/output waves can be in the range of the tens of $k_B T$. The use of phase in addition to amplitude allows us to build sophisticated three-valued logic gates and construct logic circuits with a fewer number of elements than required for conventional amplitude-based circuits.

The lack of the saturation region in the output characteristics is the major drawback inherent in interference-based devices including the Datta and Das modulator,² Mach-Zehnder spin wave interferometer,¹⁰ Magnon transistor,⁵ as well as the described magnonic interferometric switch. The integration of such devices in a large scale circuit is not feasible without the introduction of an additional non-linear device aimed to compensate inevitable variations of the output amplitude/phase. There are several possible solutions to this problem with a certain tradeoff between the circuit stability, speed, and energy consumption. For example, spin wave logic gates can be combined with nanomagnets, where the result of computation in the magnonic domain is translated into the state of magnetization.³⁹ On one hand, the combination of spin wave logic with magnetic memory may provide a route to non-volatile and imperfection prone circuits.³⁹ On the other hand, the introduction of the magnetic memory inside the spin wave logic gate will result in an additional time delay for nanomagnet switching (e.g., $\sim 1 \text{ ns}$ for conventional magnetic memory), which is orders of magnitude slower compared to the spin wave propagation time (e.g., order of ps in scaled spin wave logic gates). It is also possible to complement spin wave logic gates with parametric amplifiers providing both the amplitude and phase control of the output of each gate. In this scenario, there is no additional time delay as the parametric amplifiers can increase the amplitude of the propagating spin waves without an additional time delay. However, the additional power consumption on the parametric spin wave amplifiers may be orders of magnitude higher than the power consumption of spin wave logic gates themselves.

Finally, we want to mention that building Boolean-type logic gates is not the only, and, perhaps, not the most promising way of utilizing spin wave phenomena for data processing. The ability of using spin wave interference opens a new horizon of constructing special-task data processing devices similar to ones developed in optics but at the nanometer scale. Magnonic holographic memory is one of the examples.^{47,48} Exploiting spin wave phase in addition to amplitude also allows us to build more functional devices for pattern recognition⁴⁹ and prime factorization.⁵⁰ In turn, the combination of the conventional digital logic circuits with special type magnonic devices may pave the way for a novel hybrid digital-analog type of computing architecture.

VI. CONCLUSIONS

In this work, we considered a possibility of building spin wave interferometric switch for multi-valued all-magnonic logic gates. The switch is a three-terminal device whose operation is based on spin wave interference. The On and Off states of the switch correspond to the constructive and destructive interference, respectively. The phase of the output is exploited as an additional logic state variable. We considered examples of NOT and XOR three-valued logic gates. The operation of the scaled magnonic switch is illustrated by numerical modeling. We also presented experimental data on a micrometer scale prototype based on the $Y_3Fe_2(FeO_4)_3$ structure. The obtained data show prominent output signal modulation by the phase difference between the input spin waves. The output characteristics depend on the bias magnetic field. We present experimental data corresponding to three different orientations of the prototype in magnetic field and different configurations of the source, gate, and drain terminals. We also present the results of 15 000 subsequent measurements on the variation of the output characteristics. The On/Off ratio exceeds 13 dB at room temperature. The normalized noise spectral density S_V/V^2 determined from the output signal on the order of 10^{-11} 1/Hz indicates a possibility of low-noise low-power designs for this technology. Experimental data are complimented by micromagnetic simulations and theoretical analysis. The advantages and shortcoming of magnonic devices are discussed. Potentially, magnonic switches may be exploited for building scalable hybrid analog-digital type of computing devices.

ACKNOWLEDGMENTS

This work was supported by the Spins and Heat in Nanoscale Electronic Systems (SHINES), an Energy Frontier Research Center funded by the U.S. Department of Energy, Office of Science, Basic Energy Sciences (BES) under Award No. #SC0012670.

¹See <http://www.itrs.net/Links/2013ITRS/2013Chapters/2013ERD.pdf> for section 4.2.3 for Alternative Information Processing Devices, 7–10 (2013).

²S. Datta and B. Das, *Appl. Phys. Lett.* **56**(7), 665–667 (1990).

³K. H. Cheol, K. J. Hyun, E. Jonghwa, C. Joonyeon, H. S. Hee, and M. Johnson, *Science* **325**(5947), 1515–1518 (2009).

⁴R. J. Elliott, *Phys. Rev.* **96**(2), 266–279 (1954).

⁵M. I. D'yakonov and V. I. Perel, *Fiz. Tverd. Tela* **13**, 3581–3585 (1971).

⁶G. L. Bir, A. G. Aronov, and G. E. Pikus, *Zh. Eksp. Teor. Fiz.* **69**, 1382–1397 (1975).

⁷P. Zhang and M. W. Wu, *Phys. Rev. B* **84**(4), 045304 (2011).

⁸M. Covington, T. M. Crawford, and G. J. Parker, *Phys. Rev. Lett.* **92**(8), 089903 (2004).

⁹A. A. Serga, A. V. Chumak, and B. Hillebrands, *J. Phys. D: Appl. Phys.* **43**(26), 264002 (2010).

¹⁰M. P. Kostylev, A. A. Serga, T. Schneider, B. Leven, and B. Hillebrands, *Appl. Phys. Lett.* **87**(15), 153501 (2005).

¹¹T. Schneider, A. A. Serga, B. Leven, B. Hillebrands, R. L. Stamps, and M. P. Kostylev, *Appl. Phys. Lett.* **92**, 022505 (2008).

¹²A. V. Chumak, A. A. Serga, and B. Hillebrands, *Nat. Commun.* **5**, 4700 (2014).

¹³G. Epstein, G. Frieder, and D. C. Rine, *Computer* **7**(9), 20–32 (1974).

¹⁴A. Soltani and S. Mohammadi, *Int. J. Inf. Electron. Eng.* **3**(4), 386–390 (2013).

¹⁵G. A. Ball, W. H. Glenn, and W. W. Morey, *IEEE Photonics Technol. Lett.* **6**(6), 741–743 (1994).

¹⁶Y. Au, M. Dvornik, O. Dmytriiev, and V. V. Kruglyak, *Appl. Phys. Lett.* **100**(17), 172408 (2012).

¹⁷G. Boole, *An Investigation of the Laws of Thought on Which are Founded the Mathematical Theories of Logic and Probabilities* (Dover Publications, New York, NY, 1958, Reissued by Cambridge University Press, 2009).

¹⁸S. L. Hurst, *IEEE Trans. Comput.* **33**(12), 1160–1179 (1984).

¹⁹H. T. Mouftah and K. C. Smith, *IEE Proc. - G Circuits Devices Syst.* **129**(6), 270–272 (1982).

²⁰M. Covington, T. M. Crawford, and G. J. Parker, *Phys. Rev. Lett.* **89**(23), 237202 (2002).

²¹A. G. Gurevich and G. A. Melkov, *Magnetization Oscillations and Waves* (CRC Press, 1996).

²²C. D. Motchenbacher and F. C. Fitchen, *Low-Noise Electronic Design* (Wiley, 1973).

²³A. A. Balandin, *Noise and Fluctuation Control in Electronic Devices* (American Scientific Publisher, Los Angeles, 2002).

²⁴D. Li and P. Mazumder, *IEEE Trans. Very Large Scale Integr. Syst.* **12**(9), 910–925 (2004).

²⁵A. A. Balandin, *Nat. Nanotechnol.* **8**(8), 549–555 (2013).

²⁶J. Renteria, R. Samnakay, S. L. Rumyantsev, C. Jiang, P. Goli, M. S. Shur, and A. A. Balandin, *Appl. Phys. Lett.* **104**(15), 153104 (2014).

²⁷K. B. Klaassen, J. C. L. van Peppen, and X. Xing, *J. Appl. Phys.* **93**(10), 8573–8575 (2003).

²⁸S. Ingvarsson, G. Xiao, S. S. P. Parkin, W. J. Gallagher, G. Grinstein, and R. H. Koch, *Phys. Rev. Lett.* **85**(15), 3289–3292 (2000).

²⁹A. Khitun, M. Bao, and K. L. Wang, *IEEE Trans. Magn.* **44**(9), 2141–2153 (2008).

³⁰W. Scholz, magpar - Parallel Finite Element Micromagnetics Package Version 0.9 Build 3061M, Record No. 1012,0 (2002); available at <http://www.magpar.net/static/magpar/doc/html/index.html>.

³¹M. J. Donahue and D. G. Porter, *OOMMF User's Guide, Version 1.0 Interagency Report NISTIR 6376* (National Institute of Standards and Technology, Gaithersburg, MD, 1999). <http://math.nist.gov/oommf/>.

³²T. W. Okeeffe and R. W. Patterson, *J. Appl. Phys.* **49**(9), 4886–4895 (1978).

³³S. V. Vasiliev, V. V. Kruglyak, M. L. Sokolovskii, and A. N. Kuchko, *J. Appl. Phys.* **101**(11), 113919 (2007).

³⁴C. Kittel, *Introduction to Solid State Physics*, 8th Edition (Wiley, 2005). ISBN 978-0-471-41526-8.

³⁵M. Weissmann, A. M. Llois, and M. Kiwi, *J. Magn. Magn. Mater.* **234**(1), 19–24 (2001).

³⁶J. Weber, *Phys. Rev.* **101**(6), 1620–1626 (1956).

³⁷D. E. Nikonov, G. I. Bourianoff, and P. A. Gargini, *J. Supercond. Novel Magn.* **19**(6), 497–513 (2006).

³⁸A. Khitun and K. Wang, *Superlattices Microstruct.* **38**, 184–200 (2005).

³⁹A. Khitun and K. L. Wang, *J. Appl. Phys.* **110**(3), 034306 (2011).

⁴⁰A. Khitun, *J. Appl. Phys.* **111**(5), 054307 (2012).

⁴¹Y. Wu, M. Bao, A. Khitun, J.-Y. Kim, A. Hong, and K. L. Wang, *J. Nanoelectron. Optoelectron.* **4**(3), 394–397 (2009).

⁴²N. Sato, K. Sekiguchi, and Y. Nozaki, *Appl. Phys. Express* **6**(6), 063001 (2013).

⁴³P. Pirro, T. Bracher, K. Vogt, B. Obry, H. Schultheiss, B. Leven, and B. Hillebrands, *Phys. Status Solidi B* **248**(10), 2404–2408 (2011).

⁴⁴N. Sato, S. J. Lee, S. W. Lee, K. J. Lee, and K. Sekiguchi, *Appl. Phys. Express* **9**(8), 083001 (2016).

- ⁴⁵M. Jamali, J. H. Kwon, S. M. Seo, K. J. Lee, and H. Yang, *Sci. Rep.* **3**, 3160 (2013).
- ⁴⁶S. Klingler, P. Pirro, T. Bracher, B. Leven, B. Hillebrands, and A. V. Chumak, *Appl. Phys. Lett.* **105**(15), 152410 (2014).
- ⁴⁷A. Khitun, *J. Appl. Phys.* **113**(16), 164503 (2013).

- ⁴⁸F. Gertz, A. Kozhevnikov, Y. Filimonov, and A. Khitun, *IEEE Trans. Magn.* **51**(4), 4002905 (2015).
- ⁴⁹A. Kozhevnikov, F. Gertz, G. Dudko, Y. Filimonov, and A. Khitun, *Appl. Phys. Lett.* **106**(14), 1424091 (2015).
- ⁵⁰A. Khitun, *J. Appl. Phys.* **118**(24), 243905 (2015).